Eric L. Faulring
Chicago PT, LLC
Evanston, IL 60201 USA
eric.faulring@ieee.org

J. Edward Colgate
Michael A. Peshkin
Department of Mechanical Engineering
Northwestern University
Evanston, IL 60208
{colgate,peshkin}@northwestern.edu

The Cobotic Hand Controller: Design, Control and Performance of a Novel Haptic Display

Abstract

The design, control and performance of the Cobotic Hand Controller, a novel, six-degree-of-freedom, admittance controlled haptic display is examined. A highly geared admittance architecture is often used to render high impedances with reasonable sized actuators for a haptic display. The Cobotic Hand Controller is an extremely faithful realization of an admittance display, since it is capable of obtaining an infinite gear ratio and can render infinite impedances (up to its own structural stiffness). The incorporation of continuously variable transmissions utilizing hardened steel elements in dry-friction rolling contact provide the Cobotic Hand Controller with high bandwidth, low power requirements, and an extremely wide stable dynamic range. Here, an admittance based control algorithm for powered cobots, a novel solution to the actuation redundancy of this device, and a heuristic to avoid slip in the transmissions are described. The performance of the Cobotic Hand Controller is measured in terms of dynamic range.

KEY WORDS—haptics, admittance display, cobots, continuously variable transmission, traction drive

1. Introduction

An increasing number of virtual environment and teleoperation tasks demand high fidelity haptic interfaces. These include interaction with computer aided design models, flight simulators, telerobotic surgery, micro/nano-manipulation, undersea salvage, as well as telerobotic maintenance and decontamination and decommissioning of chemical and nuclear facilities. The execution of these tasks by a remote operator is affected by his/her level of telepresence and the transparency of the master-slave relationship (Sheridan 1992). This illusion of presence is enhanced by audio, visual and haptic cues. While visual cues are certainly mandatory, and audio cues beneficial at times, haptic cues can significantly improve the flow of information from the environment to the operator for many tasks requiring dexterity. Haptic cues are impedances; relationships between motion and force that an operator encounters when interacting with a display. It is desired that the user perceive a high dynamic range including rigid constraints and unimpeded free motion. This paper introduces a novel display that improves transparency and presence by extending the range of cues (dynamic range) that can be rendered.

The specific application for the development of the master hand controller introduced here is the teleoperation of the Dual Arm Work Platform (DAWP) at Argonne National Laboratory (Argonne National Laboratory 1998; Noakes et al. 2002). One of the key improvements the Cobotic Hand Controller can provide to DAWP operation is the implementation of virtual surfaces, or virtual constraints on motion, as suggested by Rosenberg (1994), Arai (1996), Joly and Andriot (1995), and Abbott et al. (2003). Such constraints can vastly simplify execution of a six-degree-of-freedom task in a teleoperation setting. While constraints can be implemented at the slave side in the existing system, an active master allows for the reproduction of these constraints at the master and may reduce operator fatigue while increasing efficiency by eliminating unneeded motions in six-space. Thus, if the operator is using a saw and constrains the motion of the saw to the plane of the blade at the slave, he/she feels these same constraints at the master. Rendering these constraints at the master also avoids time delay issues stemming from communication latencies.

The International Journal of Robotics Research
Vol. 25, No. 11, November 2006, pp. 1099-1119
DOI: 10.1177/0278364906072094
©2006 SAGE Publications

Existing haptic displays consist of admittance and impedance devices. Admittance displays are highly geared and therefore non-backdrivable while impedance displays have low inertia and are highly backdrivable. Admittance displays are reviewed in Hayward and Astley (1996), Carignan and Cleary (2000), and Yoshikawa (2000). The Haptic Master (Van der Linde et al. 2002) and Steady Hand Robot (Abbott et al. 2003) are notable implementations of the admittance paradigm. Although well-engineered admittance devices may have a higher dynamic range than impedance displays, they are rare due to cost and complexity. The required multi-degree-of-freedom force sensors, additional gears and bearings, and tight machining tolerances lead to significant cost. Thus the successful commercial haptic displays are often impedance devices. Impedance displays include the Phantom (Massie and Salisbury 1994), the Whole Arm Manipulator (WAM) (Salisbury et al. 1990), and many others (Force Dimension 2004; Adams et al. 1999; Quanser 2005; Adelstein and Rosen 1992; Lee et al. 2000; Millman and Colgate 1991).

While today's impedance and admittance displays may both be used to simulate a wide range of mechanical behaviors, they excel in different areas due to the nature of their control and mechanical structures. Among commercial and research devices, most serial link haptic displays have a maximum stable stiffness on the order of 1–5 N/mm (various models of the Phantom range in capability from 1–3.5 N/mm (Sensable Technologies 2006) and most parallel haptic displays have an upper stable stiffness bound of 15–50 N/mm (Force Dimension 2004; Kim et al. 2003). A stiffness of 1 N/mm is generally accepted as the minimum required to convey the presence of a constraint. Greater than 24 N/mm is required to convey the presence of a "hard" or "rigid" constraint (Tan et al. 1994). Impedance displays can have an unmasked inertia as low as 0.05 kg, while admittance displays typically have a minimum stable mass of 2–5 kg. Impedance displays are well-adapted to simulating low inertia, low damping environments, but have difficulty rendering energetically passive stiff constraints (Hannaford 1989b; Brown and Colgate 1997). On the other hand, admittance displays are well-adapted to displaying rigid constraints but struggle to simulate unencumbered motion. Unlike impedance displays, admittance displays must actively mask inertia and damping, which are their inherent physical behaviors due to their non-backdrivable transmissions.

1.1. Cobots

The word *cobot* is derived from collaborative and robot, meaning shared control between a human operator and a computer (Colgate and Peshkin 1999a, 1999b). Cobotic devices control the relative velocities of their joints by modulating continuously variable transmissions (CVTs) with small steering actuators (Figure 1). Cobotic CVTs have been developed to relate two translational velocities, two rotational velocities, or a rotational velocity to a translational velocity, and have been used in many prototype devices (Peshkin et al. 2001; Gillespie et al. 2001; Moore et al. 2003; Wannasuphoprasit et al. 1997). The velocity ratios enforced by constraints in the transmissions cause cobots to have only a single mechanical instantaneous motion freedom, regardless of the dimension of their configuration space. The dynamics along this single instantaneous motion freedom defined by the CVTs are controlled via a single power injector in an active cobot such as the Cobotic Hand Controller, or by a human operator in the case of a passive cobot. Rolling constraints in the transmission elements, not electrical power, resist forces orthogonal to the current motion direction. The transmissions draw power from a single common element actuator as needed, potentially reducing the weight and power requirements of the overall mechanism. Using a continuously variable cobotic transmission can eliminate the need to make compromises on output flow and effort, which are inherent in choosing a fixed transmission ratio, and also allow the common element actuator to be operated at an efficient speed nearly all of the time. In addition, the cobotic architecture allows for the ability to both lock or decouple joints without any additional actuators beyond the single low-power steering actuator for each CVT.

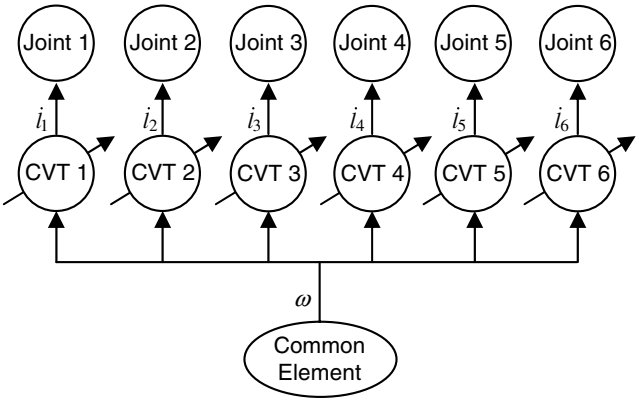

Fig. 1. Parallel cobotic transmission architecture. While there are six joint speeds that must be controlled for the Cobotic Hand Controller to render a virtual environment, there are six CVTs and a power cylinder (common element) that must be actuated. It is arbitrary at what speed to have the power cylinder moving since it is related via CVTs to the joints.

1.2. Summary of paper

In Section 2 we provide a detailed description of mechanical design of the Cobotic Hand Controller recently introduced by Faulring et al. (2004, 2005). In Section 3 we review the computation of forward and inverse kinematics for the device. In Section 4 we review the workspace, mechanism stiffness,

force limits and the backdrivability of the device. In Section 5, we summarize our virtual environment admittance control algorithm and outline the overall control strategy and low level controllers. A heuristic is developed that limits slip in the CVTs and therefore protects against instability of the display. In Section 6 we derive a novel methodology for dealing with the actuation redundancy of the display. In Section 7 we analyze the acceleration ability of the display. In Section 8 we analyze the dynamic range of the Cobotic Hand Controller. Finally in Section 9 we provide conclusions and suggestions for future investigations.

2. Design

2.1. Geometry

The design of the six-degree-of-freedom Cobotic Hand Controller, shown in Figure 2, utilizes the kinematics of a parallel platform introduced by Merlet (1991, 1992). The parallel platform portion of the geometry (i.e., everything but the cylinder and wheels) has also been used in an ophthalmic surgery robot developed by Grace (1995) and, in a slightly modified form, in an industrial dextrous assembly robot called the Paradex (Morris 2001). The proximal links are coupled by three-degree-of-freedom universal joints to the distal links, and these in turn are coupled via two-degree-of-freedom universal joints to an end-effector platform. Here a multi-axis force sensor is placed to measure the user's intent. Our addition to Merlet's kinematics is to relate the six linear actuators to a central power cylinder through non-holonomic rolling constraints. An alternative CVT design for a six-degree-of-freedom cobot was proposed by Emrich and Hodgson (2000).

Linear actuation of the proximal links is achieved by a rotational-to-linear continuously variable transmission (CVT), namely a steered wheel. The steering angle of each wheel relates the linear velocity, $\dot{l}_i$, of each proximal link to the rotational velocity, ω, of the power cylinder. A linearly moving carriage, shown in Figure 3, couples each CVT wheel to each proximal link. When the wheels are steered such that their rolling axis is parallel to the power cylinder's ($\phi_i = 0$), a ratio $\dot{l}_i = -R\omega \tan\phi_i = 0$ is set. If the wheels are steered in either direction from $\phi_i = 0$, ratios between $\pm$ infinity can be achieved. In practice, wheel slip limits this range. It is also evident that turning all six wheels to $\phi_i = 0$ locks the six actuators, and turning them to $\phi_i = \pi/2$ completely decouples the actuators from the cylinder's velocity, although the cylinder would then be unable to turn.

The cobot was designed for some degree of kinematic flexibility. Thus the offset clamps (Figure 2) adjoining proximal and distal links have two attachment points for the distal links and can be rotated about the proximal links. Rotating them inward yields a larger rotational workspace but reduced stiffness. The mounting positions of the distal universal joints to the end-effector plate are adjustable as well. In addition, the

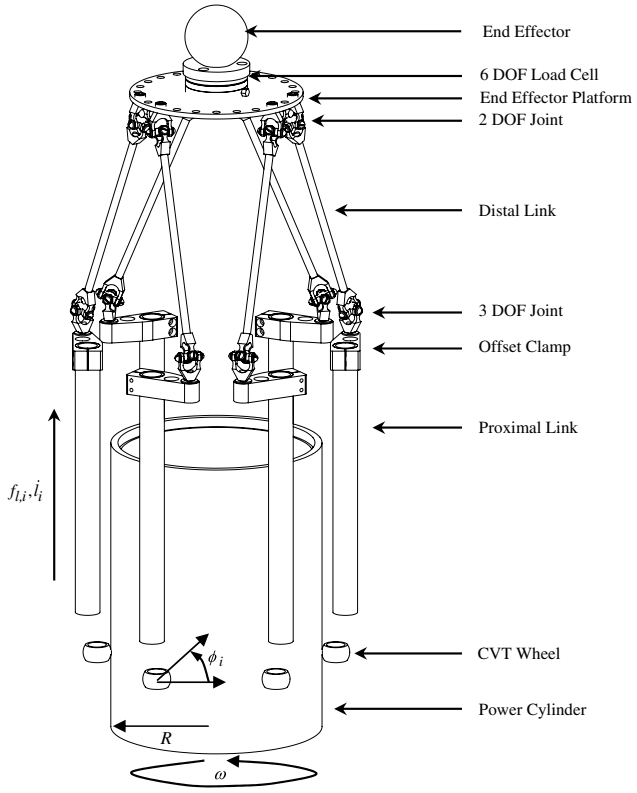

Fig. 2. The kinematics of a Merlet-cobotic parallel platform (not to scale - the proximal links and cylinder have been shrunk by about 40 percent in length relative to the distal links). This design consists of six linear actuators arrayed around a central power cylinder. Later figures detail the structure connecting the wheels to the proximal links.

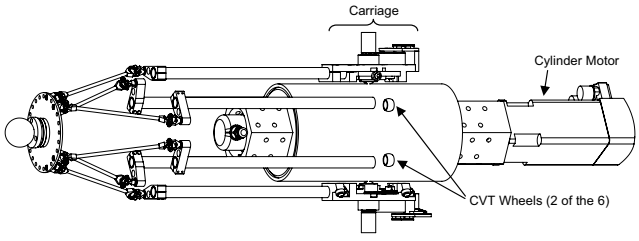

Fig. 3. In this figure, the motor driving the cylinder is explicitly shown. Two of the steering wheels are exposed. Carriages relating two other wheels to their proximal links are visible.

length of the distal links is easily changed as they are made of threaded rod that inserts directly into the universal joints.

The universal joints themselves are unusual in that they exhibit continuous rotation even when coupling shafts that are almost perpendicular (87.5 degrees). This severe operation angle would be detrimental if they needed to transmit power rotationally, but here they need only to transmit power through translation of the universal joint as they maintain a kinematic constraint. They were designed and built specifically for the Cobotic Hand Controller and each contains four preloaded radial bearings.

As shown in Figure 4, the two ends of the device are capped by endplates which sit in v-groove rollers. Thus the whole device can be rotated and fixed by a locking pin at increments of 30 degrees for maintenance or kinematic purposes. Each of the carriages can be removed independently if the proximal-distal offset clamp is detached. Wire management guides all wiring (not shown) through the rear endplate. The whole cobot can be turned upright and operated with the cylinder oriented vertically, although significant power (and a fraction of the preload at the wheel) would be consumed to move the joints against gravity.

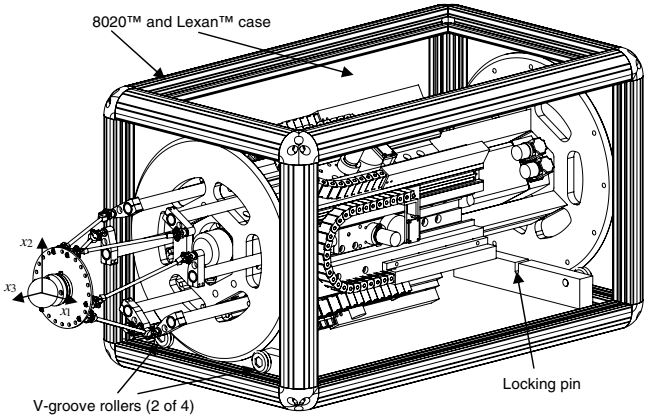

Fig. 4. A CAD rendering of the cobot in its protective case. The cobot is cradled in v-groove rollers to allow easy repositioning of the device for maintenance or kinematic purposes. Task space coordinate frame X is located at the center of the manipulandum's workspace.

2.2. Joint assemblies

The parallel nature of the Merlet-cobotic mechanism allows for six identical actuator assemblies. As shown in Figure 2, there are six equally spaced proximal links and actuator assemblies. These assemblies, depicted in Figure 5 and detailed in Figures 6–10, are bolted to a central core, detailed in Figure 11.

All structural components are machined from aluminum with the exception of the proximal links. These are 15.875 mm diameter ceramic tubes chosen for their high strength to weight and stiffness to volume ratios. The ceramic tubes at their current length provide 24 cm of workspace along the axis of the cylinder. The upper limit of the workspace is limited by the cylinder's 25 cm length. The moving portion of each joint assembly (depicted in Figure 6) has mass $m_l = 0.9$ kg.

A conductive-plastic linear potentiometer (see Figure 7) was chosen as a continuous linear sensor over numerous digital incremental options due to its lightweight untethered wiper, as well as for the ability to perform analog differentiation of its output in order to obtain a high resolution velocity signal. Although the circuitry and code were developed to interpret this analog differentiated signal, the signal-to-noise ratio is such that the finite-differentiated and digitally filtered position signal yields an equally good velocity signal.

Figure 8 details the linear guideway chosen. It was designed to minimize the friction in and construction tolerances required for the linear guideway. In addition, we desired to locate the CVT wheel, which is preloaded against the power cylinder, between the two guide rods in order to avoid requiring the guideway to resist significant moments. The resulting

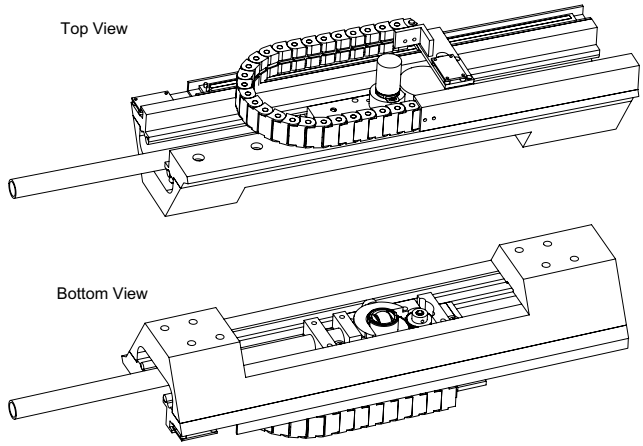

Fig. 5. Top and bottom isometric views of a linear actuation assembly.

design utilizes two guide rods and five rollers, four of which are aligned against one guide rod, the fifth against a second guide rod. The sixth point of contact, which constrains the carriage to one or zero degrees of freedom depending on the steering angle, is provided by the cobotic steering wheel.

There are several key advantages of this non-overconstrained design over commercially available alternatives. Notably, the guideway does not over-prescribe the linear motion of the carriage, and operates without binding (locking up) even if the

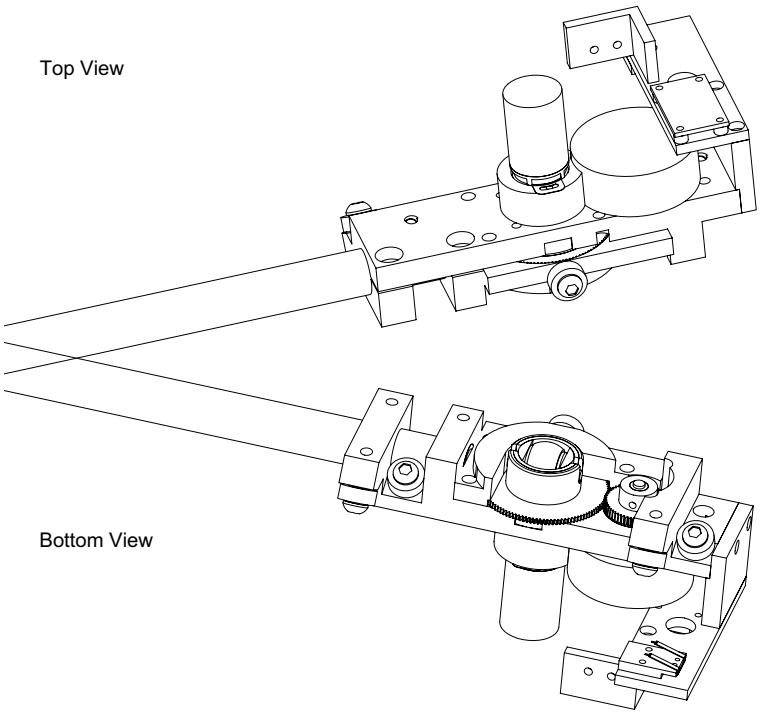

Fig. 6. Top and bottom isometric views of a carriage and proximal link, which make up the moving portion of the linear actuation assembly.

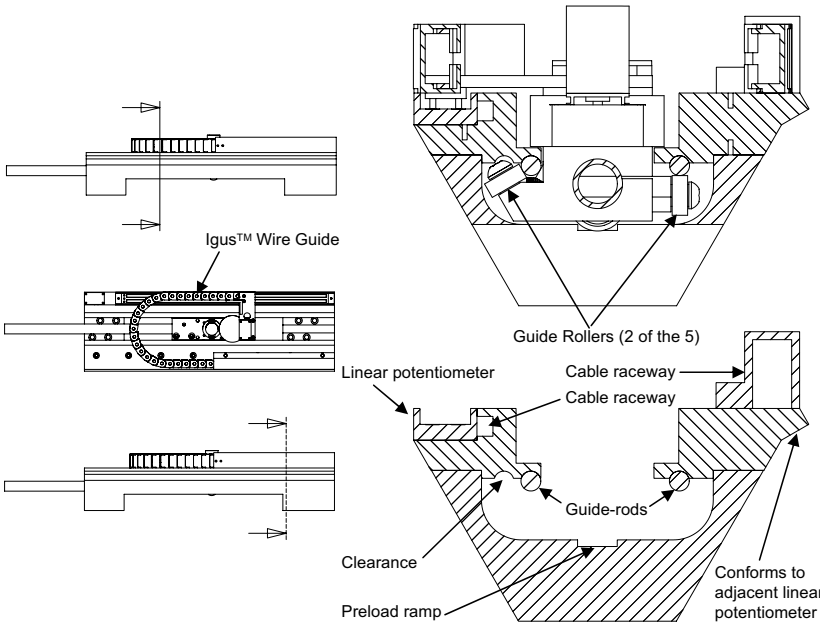

Fig. 7. Shown is one of six identical actuator assemblies. The proximal link is grounded to a carriage on a linear guideway. An Igus™ flexible wire guide manages wiring for the steering motor and encoder. A ramp allows the carriage to be inserted between the guide-rods and cylinder, with the spacing decreasing gradually as the CVT wheel approaches the cylinder. This allows the application of a preload force by compressing springs within the steering bell (see Figure 10).

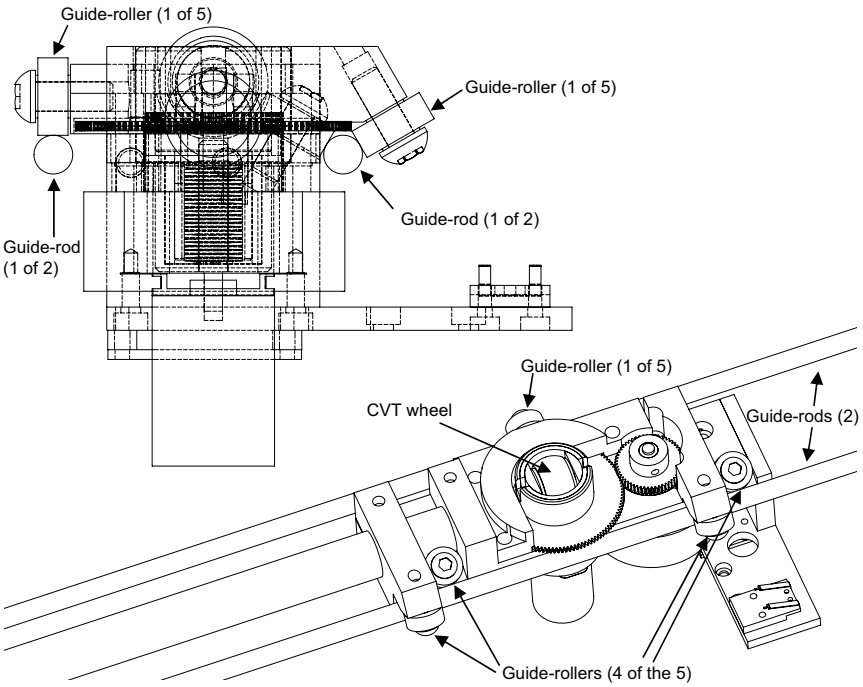

Fig. 8. Removing the supporting structure of the linear actuation assembly in Figure 5 reveals steel guide rods for linear motion. The linear bearing consists of five cam-follower studs, two guide-rods and the CVT wheel.

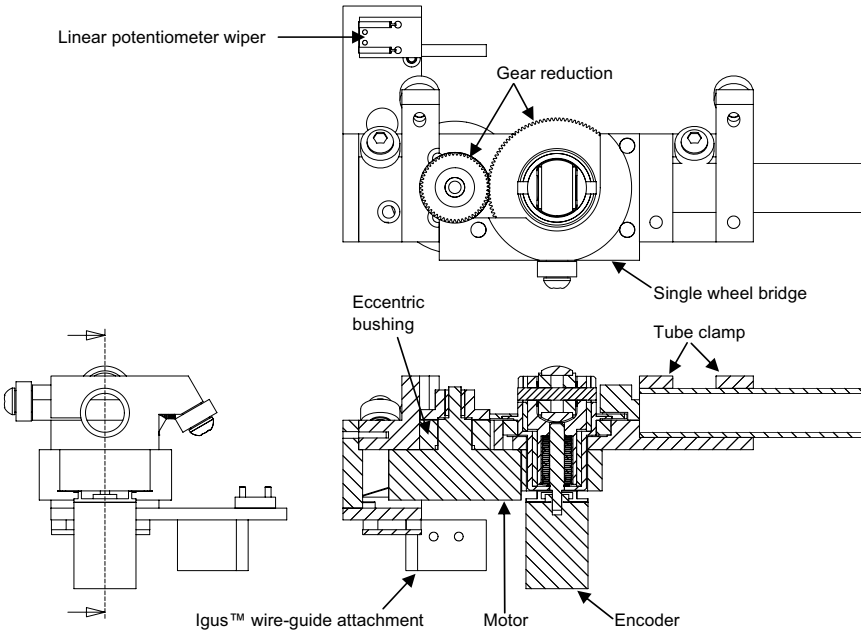

Fig. 9. Carriage features. Each carriage relates a CVT wheel to a proximal link. It houses the steering motor which drives the steering bell assembly via a single-stage gear pair. An eccentric bushing allows fine adjustment of the inter-gear spacing.

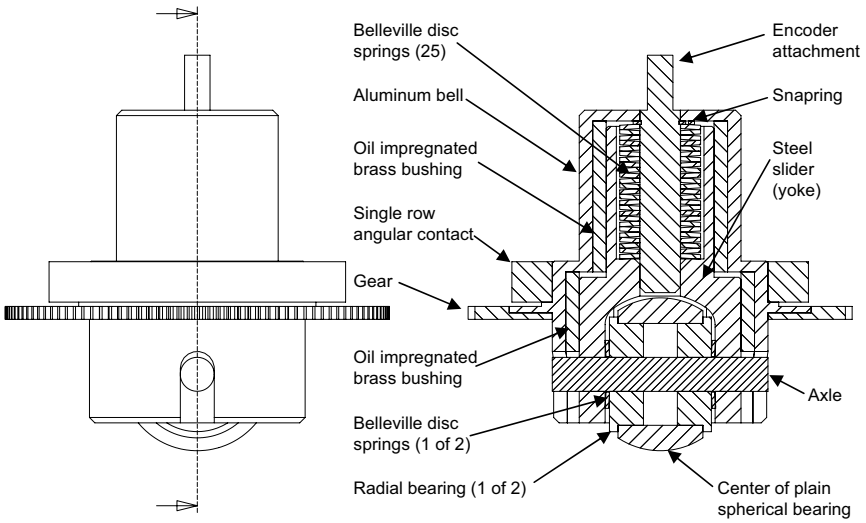

Fig. 10. Steering bell features. The yoke supports the CVT wheel axle and is able to slide freely within the bell, guided by the brass bushings normal to the cylinder. If the distance between the linear guideway and cylinder changes over the stroke length, the Belleville springs absorb the change in position of the yoke while maintaining a preload. The wheel axle intersects the bell and causes the wheel to steer as the bell is driven by a gear pressed around it.

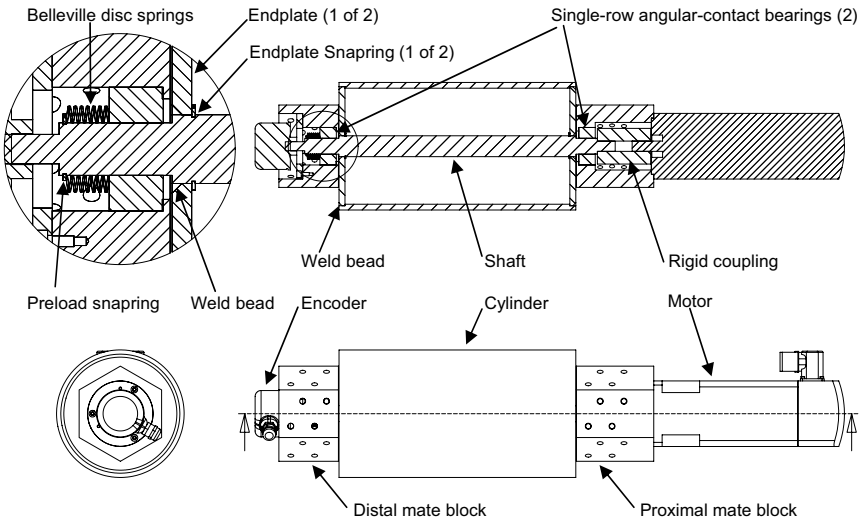

Fig. 11. A power motor drives the power cylinder. The cylinder shell is welded to its endplates and these to the shaft. A series of Belleville disc springs load the cylinder bearings.

two guide rods are skew or are bent by significant loading. The guideway is preloaded by the same mechanism that loads the CVT wheel against the power cylinder. As the preload at the wheel is increased, so does the ability of the linear guideway to resist wrenches on the proximal link without shifting. This effect coincides with the desire for the wheel to provide higher constraint forces. An adjustable preload is provided by placing approximately 25 Belleville disc springs (see Figure 10), in some combination of parallel or series, between the yoke of the CVT wheel and its housing. The spring-constant for this set of Bellevilles needs to be such that as the carriage travels from one end of the cylinder to another, minor changes in the length of the spring ($\pm 50\mu$m) do not significantly alter the preload, since the preload will affect the dynamics of steering, linear motion control and cylinder control. Also mounted on the carriage is an optical encoder for measuring steering angle, a steering motor coupled via gears (2.33:1) to the steering bell and a wiper for a linear potentiometer (see Figure 9).

Designing wheels for use in cobots has always been problematic. Conflicting design goals when choosing wheel materials has limited wheel performance. It is desired that the wheels provide a high transverse frictional force with minimal preload, yet it is also desired that the wheels have low steering friction in order to allow for smaller steering actuators and higher bandwidth of control. It is also desired that the wheels have low rolling friction and little dissipation in order to provide for backdrivability and a reduced power requirement for powered cobots. The wheel should not have any compliance transverse to the rolling direction if a rigid transmission is desired. Finally the wheel material should incur minimal wear due to steering or rolling.

Previous cobots have typically utilized polyurethane Rollerblade™ wheels (75 mm in diameter) in order to obtain the necessary transverse coefficient of friction. For the Cobotic Hand Controller we chose to move to harder wheel materials to increase the stiffness and bandwidth of the device, and to reduce rolling losses. Also, the linear guideways required the existence of a high preload (unnecessary for the high friction polyurethane wheels). With these two constraints in mind, steel wheels (18 mm diameter) were chosen to run against a steel power cylinder even though the coefficient of friction of steel on steel is an order of magnitude less than that of polyurethane on steel. Depending on performance needs (transverse friction or resisting of wrenches on the guideway), more or less preload can be utilized. Currently the preload P is set to around 250 N. The CVT wheels start out with a spherical profile and are the centers of plain spherical bearings with a hardness of Rockwell C 58. After a few hours of use, the wheels, originally with a black-oxide coating, have a shiny flat strip 880 μm across. Even after 12 months of intermittent use in the lab, the strip is no larger than 910 μm across, which amounts to a total of 11 μm of wear off the radius of the wheel. We find the coefficient of friction, μ, for support of lateral forces between the steel wheels and steel cylinder, to be around 0.12. This is the point at which lateral creep breaks down into gross slip.

2.3. Power Cylinder

As shown in Figure 11, the power cylinder is located between two mating blocks. The steel cylinder is 25 cm in length, 13.64 cm in diameter, and has a 6.25 mm wall thickness. The cylinder shell has been welded to its end-caps, and these to the shaft (total inertia of 0.0286 kgm^2). The cylinder/end-caps/shaft were then hardened to Rockwell C 59.8 and cylindrically ground between centers to a 12 μinch finish. In 12 months of use, the cylinder has not shown evidence of wear.

Each of the six linear actuator assemblies bolt to the mating blocks. Also connected to the blocks are the power motor and a high resolution encoder. The motor is connected via a rigid coupling to the cylinder. A flexible coupling was originally present, but later removed to avoid unwanted resonances. A large 1200 watt motor was chosen as it was readily available in the lab and had sufficient torque to operate without gearing. The original goal of the large motor was to mitigate backlash, thus allowing smooth operation including reversal of direction, and to allow backdrivability if the system was ever operated passively. Ultimately, control algorithms were never implemented to take advantage of this feature, and preload and speed limitations have only allowed us to draw about 60 watts of mechanical power from the cylinder motor, 5% of its capacity. Assuming we had a 70% efficient gear-train between a much smaller motor and the cylinder, a motor capable of peaking at 86 watts would have sufficed to drive the cylinder.

2.4. Electronics and Software

Table 1 summarizes the specifications of the sensors and actuators. All motors are brushless DC operated in torque (current) mode. The linear position and force are recorded via 16 bit ADC boards. All the necessary electronics, including motor amplifiers and power supplies, the control computer, and signal conditioning hardware were placed in a single cabinet measuring $41 \times 46 \times 53$ cm. The control computer is comprised of a 1.53 GHz standard personal computer running the QNX 6.2 real-time operating system. An oscillator and counter, on one of three data acquisition boards, is used to generate hardware interrupts at approximately 2000 Hz, to which all data acquisition and output is latched electronically. Board IO and algorithms that run at the full 2000 Hz take about 60 μs and 220 μs respectively. Writing data to disk, network communication and updating the GUI are performed at lower rates, and are lower priority threads. All code was written in C.

3. Kinematics

The Cobotic Hand Controller has two discrete sets of kinematics, the first general to robotic devices and the second

Table 1. Sensor and Actuator Specifications

Sensor	Resolution	Linearity	Range
Power Cyl Enc	140,000 cnts/rev	NA	2π
CVT Encoders	40,960 cnts/rev	NA	2π
Linear Pots	16 bit ADC (5μm)	1/2000	300 mm
Force-Torque	16 bit ADC (2.5 mN)	1/3000 ($\pm$ 5N), 1/70 ($\pm$ 40N)	$\pm$40 N,$\pm$2 Nm
Actuator	**Peak Torque**	**Cont Torque**	**Wattage**
Power Cyl Motor	13 Nm	3.7 Nm	1200*
CVT Motors	260 mNm	54 mNm	30

*This oversized motor was chosen as it was readily available and eliminated the need for gearing and the associated backlash and nonbackdrivability. Ultimately control modes never took advantage of these features, and only 60 mechanical watts have ever been asked of the cylinder motor.

specific to cobots. The first set of kinematics transforms between the $SE(3)$ rigid body motion of the end-effector (task space) and the $\mathbb{R}^6$ straight-line motion of the six proximal links (joint space). The second set of kinematics transforms between joint space and steering space, as a function of cylinder speed.

3.1. Joint-to-task Kinematics

Let us define as the joint-to-task forward kinematics of the parallel platform portion of the Cobotic Hand Controller as the functions, $\vartheta(l)$, that take us from joint space coordinates, l, to task space coordinates,

$$x = \vartheta(l), \tag{1}$$

of the manipulandum (end-effector). The Jacobian, J, relates motion in joint space, $\dot{l}$, to motion in task space, $\dot{x}$.

$$\dot{x} = J(l)\dot{l} \qquad J(l) = \frac{\partial \vartheta(l)}{\partial l} \tag{2}$$

The manipulandum coordinates are given by three translational coordinates (x_1, x_2, x_3) and three Euler angles (x_4, x_5, x_6). We have chosen a Euler angle set such that all singularities are outside of the workspace for our specific manipulandum. Euler angles allow us to work in generalized coordinates rather than with the special orthogonal group $SO(3)$.

3.1.1. Inverse Kinematics

Inverse kinematics are deduced by relating an end point position, x, in task frame coordinates to the joint space extensions, l. Equations for the known fixed lengths of the proximal links are employed. This is equivalent to $l_i = \vartheta_i^{-1}(x)$. While we do not have an analytical expression for $J(l)$, its inverse $J^{-1}(x) = \frac{\partial \vartheta^{-1}(x)}{\partial x}$ is easily established from the expressions $l_i = \vartheta_i^{-1}(x)$, and relates velocities $\dot{l}$ and $\dot{x}$.

$$\dot{l} = J^{-1}(x)\dot{x} \qquad J_{ij}^{-1}(x) = \frac{\partial \vartheta_i^{-1}(x)}{x_j} \tag{3}$$

A series of six, 6×6 Hessian matrices $H_i^{-1}(x)$, $i = 1 \ldots 6$, can also be established that expose individual joint accelerations $\ddot{l}_i$ from general task space accelerations $\ddot{x}$.[1]

$$H_{i,jk}^{-1}(x) = \frac{\partial^2 \vartheta_i^{-1}(x)}{\partial x_j \partial x_k} \tag{4}$$

$$\ddot{l}_i = \sum_{j=1}^{6} J_{ij}^{-1}(x)\ddot{x}_j + \sum_{j=1}^{6}\sum_{k=1}^{6} H_{i,jk}^{-1}(x)\dot{x}_k\dot{x}_j$$

3.1.2. Forward Kinematics

For the general case of a six-degree-of-freedom parallel manipulator, if no pairings (intersections of axes of universal joints) exist at the platform or base, a closed form analytical solution is not available for the forward kinematics. In fact, twelve solutions are possible for task space coordinates for a given set of joint coordinates without using any heuristics about collisions or range of motion. In practice, a Newton-Raphson iterative scheme can be used to compute the task space coordinates, x, given measured joint coordinates, l, and an initial estimate for the task space coordinates, x_o. However, it will become apparent that knowledge of the actual task space coordinates is unnecessary and the Newton–Raphson scheme is not needed. The Cobotic Hand Controller tracks a desired

1. At runtime the inverse Jacobian (36 terms) and the Hessians (216 terms, 90 of which are unique and non-zero) are computed analytically at each time step. The Jacobian $J = (J^{-1}(x))^{-1}$ is also computed via a numerical routine. The Jacobian is needed to map forces from task to joint space in order to compute a feedforward cylinder torque.

trajectory in task space and we map this desired position, velocity and acceleration to joint space. This is done by utilizing a Jacobian and Hessian computed from the desired task space location. Then our feedback control is implemented in joint space. Thus we do not need to map the actual joint space location to task space via a Newton–Raphson scheme.

3.2. Steering-to-joint Kinematics

Let us define as the steering-to-joint forward kinematics of the continuously variable transmission portion of the Cobotic Hand Controller as the functions that take us from steering angle, ϕ_i, and cylinder speed, ω, to joint space velocity, $\dot{l}_i$.

3.2.1. Forward Kinematics

The input and output flows for each rotational-to-linear transmission are related via

$$\frac{\dot{l}_i}{\omega} = -R\tan(\phi_i). \tag{5}$$

Here we have neglected flow losses due to elastic creep in the transmission which we model in Faulring (2005) and Faulring et al. (2006b).

3.2.2. Inverse Kinematics

During operation of the display, we seek to control joint motion, and thus the appropriate steering velocities are computed given the commanded joint accelerations. We differentiate Equation 5 and obtain

$$\dot{\phi}_i = -\frac{\ddot{l}_i + R\dot{\omega}\tan(\phi)}{R\omega\sec^2\phi_i}. \tag{6}$$

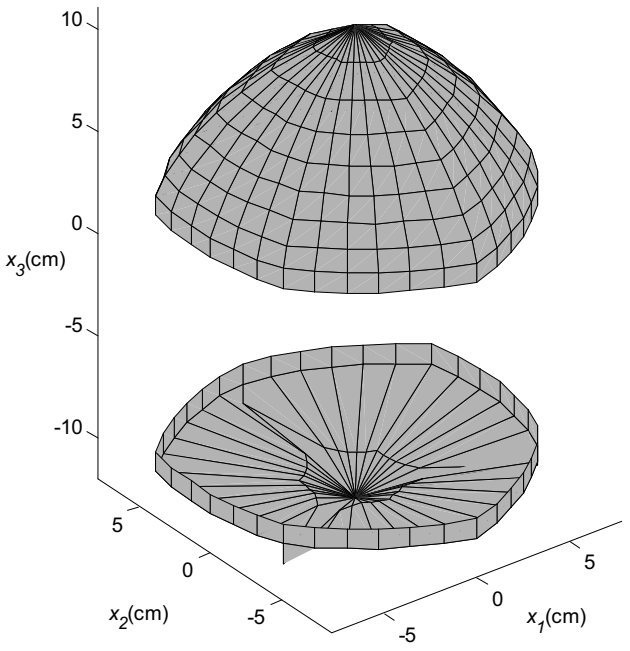

Fig. 12. Translational workspace without allowing rotation. The workspace is best approximated by an 8 cm radius hemisphere stacked on top of a 16 cm diameter, 13 cm long cylinder, oriented along the x_3 direction (see Figure 4 for the coordinate directions). Thus the workspace has a relatively flat bottom and a domed top. The three-fold symmetry of the proximal-distal link connection points is apparent in the grooves on the bottom, and in the slightly hexagonal shape of the cylinder and dome.

4. Characterization

In this section we describe the translational and rotational workspace, the mechanism stiffness and resonant modes and the output force limitations due to finite preloads. We also provide a description of the backdrivability of our current implementation of the display.

4.1. Workspace Analysis

Situations that limit the workspace of the Cobotic Hand Controller are distal-joint to distal-link collisions, distal-link to platform singularities (occurring when the link lies parallel to the platform), distal-link to proximal link singularities (occurring when the links are orthogonal), proximal link stroke range, and universal joint operation range. These limits are from a collision and singularity standpoint only, and do not take into account manipulability or stiffness. Projections are needed in order to portray the six-dimensional workspace in two or three dimensional plots. We follow Wang (1999) and Chuckpaiwong (2001) who provide workspace analyses of the Paradex manipulator, a device with similar kinematics to the Cobotic Hand Controller. In Figure 12 we show the translational workspace of the Cobotic Hand Controller provided no rotations are permitted. In Figure 13 we show the rotational workspace of the Cobotic Hand Controller provided no translations are permitted.

4.2. Mechanism Stiffness

Structural stiffness of the Cobotic Hand Controller is high for a haptic display. Stiffness is approximately 400 N/mm throughout the workspace along the cylinder's axis. Structural stiffness orthogonal to the cylinder axis ranges from 50 N/mm in the center of the workspace to 20 N/mm away from the cylinder's axis and rotated at extreme angles. The stiffness goes to zero in one or more degrees of freedom when the Jacobian becomes singular (i.e., a distal link is parallel to the end-effector platform or a distal link is perpendicular to its proximal link). These measurements were made by loading

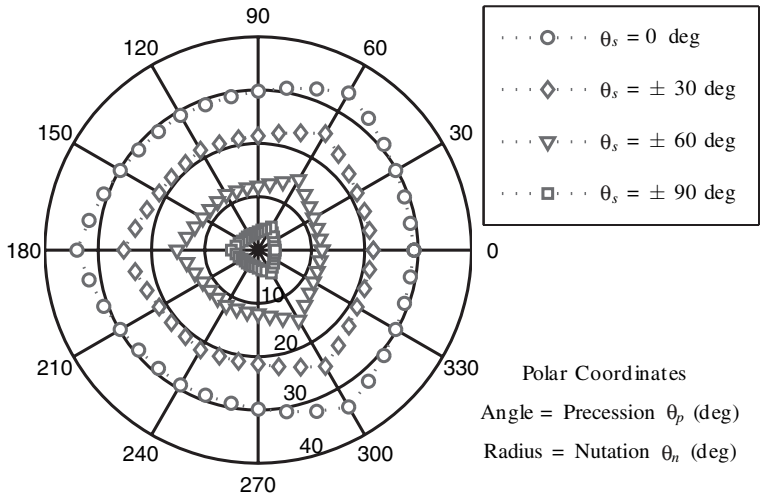

Fig. 13. Rotation workspace without allowing translation. Nutation θ_n is the angle by which the end-effector is tilted away from the x_3 axis of the central cylinder (see Figure 4). Precession θ_p is the direction in which the nutation occurred. Spin θ_s is the spin of the end-effector about the nutated and precessed axis. The various contours on the polar plot are for different fixed amounts of spin, with the radius of the contour indicating the amount of nutation, and the angle of the contour the precession. If we desire spin $\theta_s = \pm 90$ degrees, the amount of nutation allowed is only 2–3 degrees, depending on the direction of precession. If we only desire spin $\theta_s = \pm 30$ degrees, the amount of nutation allowed is 22–25 degrees, depending on direction of precession.

the platform with a spring-scale and measuring deflections with a dial indicator.

We also predict the potential bandwidth of the Cobotic Hand Controller by examining the resonant modes of its lengthy mechanical linkages. Assuming a 0.5 kg end-effector is coupled to a beam with the previous stiffness measurements, the 400 N/mm stiffness along the cylinder's axis yields a 142 Hz mode. A 0.5 kg end-effector coupled to a 50 N/mm spring yields a 50 Hz mode. Impact excitation experiments confirm these estimates. The Cobotic Hand Controller's first resonant mode orthogonal to the cylinder axis is around 60 Hz, followed by additional content at 120–150 Hz and 300 Hz. The 60 Hz mode is not present along the cylinder axis, although 120–150 Hz and 300 Hz content is present.

4.3. Limits due to Preload

An analysis of the forces at the contact patch of the wheel is critical for determining the performance limits of the Cobotic Hand Controller. The input and output efforts of the rotational-to-linear transmission are related by

$$\frac{f_{w,i}}{\tau_c} = -\frac{1}{R\tan(\phi_i)} \tag{7}$$

and are diagrammed in Figure 14. $f_{w,i}$ is the net force applied by the cylinder on the wheel in the joint direction. τ_c is the cylinder torque acting on the wheel. Here we have neglected the effort losses due to rolling friction in the transmission and the CVT wheel axle bearings which we model in Faulring (2005) and Faulring et al. (2006a). The output force of the joint at the wheel,

$$f_w = m_l\ddot{l} + c_{d,l}Psgn(\dot{l}) - f_l, \tag{8}$$

is composed of the inertial force of the joint, $m_l\ddot{l}$, the joint friction force, $c_{d,l}Psgn(\dot{l})$, and the net output force of the joint, f_l (the operator applied force). $c_{d,l}$ is the linear guideway dynamic coefficient of Coulomb friction. For preload force P set to 250 N, joint friction $c_{d,l}Psgn(\dot{l})$ is 0.84 N. The joint masses m_l are 0.9 kg.

Forces in the longitudinal (rolling direction) of the wheel are essentially zero, unless the wheel is accelerating, or experiencing rolling friction. The net lateral force, $f_w \sec\phi$, is of primary concern. Adequate lateral friction force, μP, must be present so that

$$\mu P \geq f_w \sec\phi. \tag{9}$$

When this is satisfied, adequate friction force is available to accelerate the linear carriage, to combat joint friction and to apply the net force, f_l, to an operator. With all transmissions steered to $\phi = 0$, thus attaining their maximum available lateral friction forces $\mu P/sec(\phi) = 30$ N, the combined six

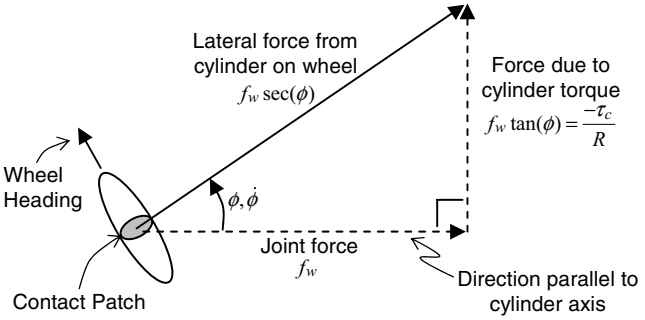

Fig. 14. Forces from cylinder acting on the wheel at the contact patch.

joints of the Cobotic Hand Controller can sustain task space loads of ≥ 50 N without the expense of any electrical power.

4.4. Backdrivability

Here we examine first the inertial forces and then the friction forces that a user feels when attempting to backdrive a passively operated Cobotic Hand Controller.

4.4.1. Apparent Inertia

Due to the rolling constraints in the transmissions, the cobot only has a single motion freedom for a given set of steering angles, and the apparent inertia of the cobot along this single motion freedom incorporates the six joint masses as well as the cylinder inertia, in some combination depending on the transmission ratios. The lowest the apparent inertia could be in the translational direction along the cylinder's axis is $6m_l = 5.4$ kg, the sum of the six joint masses, plus the steering angle dependent contribution of the cylinder inertia which can be zero for $\phi = \frac{\pi}{2}$, or infinite for $\phi = 0$. Apparent rotational inertias at the end-effector are on the order of 0.005 kgm^2 or greater. The rendering of lower translational or rotational inertias requires a powered cobot to mask the apparent inertia.

4.4.2. Friction

In order to backdrive the Cobotic Hand Controller, an operator has to overcome joint guideway friction, rolling friction at the wheel–cylinder interface and friction in the wheel and cylinder bearings. The joint frame force due to guideway friction is $c_{d,l} Psgn(\dot{l})$ for each joint. The joint frame force needed to backdrive the CVT wheels is $\frac{\tau_{w,fr}}{r \sin(\phi)}$ for each wheel, where r is the radius of a CVT wheel and $\tau_{w,fr}$ the rolling friction torque from inelastic losses at the wheel–cylinder interface and the friction in the wheel axle bearings. The joint frame force needed to backdrive the cylinder bearings is $\frac{\tau_{c,fr}}{R \tan(\phi)}$. These quantities have been estimated analytically and evaluated experimentally by Faulring (2005) and are $c_{d,l} Psgn(\dot{l}) = 0.84$ N, $\tau_{w,fr} = 0.001$ Nm and $\tau_{c,fr} = 0.084$ Nm. If all the wheels are steered at $\phi = \frac{\pi}{2}$ such that the cylinder does not spin, an operator would have to apply effort 5.7 N in order to backdrive the six joints. If the wheels were steered at $\phi = \frac{\pi}{4}$, an operator would have to apply 7.23 N of effort. The rendering of forces lower than these frictional forces requires a powered cobot.

5. Control

When controlling a passive cobot interacting with a haptic environment, researchers have typically thought in terms of the extreme cobotic behaviors, *freemode* and *virtual-surface* mode. With regards to the powered and parallel (redundantly actuated) Cobotic Hand Controller, the delineations between freemode and virtual-surface mode are blurred, and a completely different strategy can be adopted. The strategy we use commands desired accelerations in all directions. In Faulring (2005) and Faulring et al. (2006b) we develop such a strategy for the general admittance controlled device. Our methodology is capable of displaying the proper dynamics for any desired inertia matrix both tangent and orthogonal to the current motion freedom. In addition, the rendering of holonomic and/or nonholonomic constraints is supported and examples are provided in Faulring (2005) and Faulring et al. (2006b).

In the following, we first examine a one-degree-of-freedom system, or a single joint of our display. We leave out the joint-to-task kinematics until Section 5.5. The overall control scheme for this single-joint Cobotic Hand Controller is diagramed in Figure 15. This scheme consists of a one-degree-of-freedom *virtual environment* or dynamics simulation that computes desired accelerations in response to measured interaction forces with the human operator. The dynamics simulation is described in Faulring (2005) and (Faulring et al. 2006b) where we demonstrate the Cobotic Hand Controller's ability to render high degree-of-freedom constraints. The dynamics simulation contains an integrator and, therefore, is capable of feeding forward position, velocity and acceleration commands to the cobot, which executes motion control at the joint level. The cobot plant contains a power cylinder plant and a steering plant. The cobot renders motion to the human operator, and receives a force in response. Throughout the remainder of this section, we break down Figure 15 into increasingly smaller elements and analyze them in detail.

5.1. Joint Motion Control

The *joint motion control* block is a feedback controller to insure that the measured joint position l'_v tracks the reference, l_r. This consists of a PID feedback controller and a feedforward component. The derivative term makes use of a joint velocity estimate $\dot{l}' = R\omega' \tan(\phi')$, computed from cylinder speed and

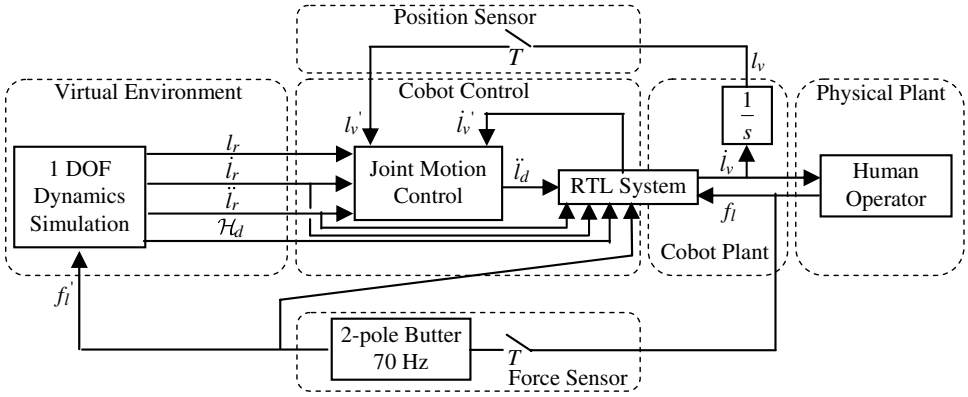

Fig. 15. The overall control diagram without kinematics (for a single leg). The $'$ notation indicates sampled (measured) signals.

steering angle rather than by differentiating linear position.[2] The output of this controller is a desired joint acceleration, $\ddot{l}_d$. Even in the full six-degree-of-freedom plant, feedback on motion control is still implemented at the joint level (as opposed to operational space feedback). This makes the tuning of gains simple by rendering the tuning of disparate rotational and translational feedback gains unnecessary. A disadvantage of feedback in joint space is that the dynamic response in task space is no longer linear, after the kinematics of the universal joints and distal links. The closed loop joint motion controller has 45 degrees of phase lag at its 40 Hz bandwidth point.

5.2. Rotational-to-Linear System

The *rotational-to-linear* (RTL) block (Figure 16) contains the cylinder and steering plants and controllers that make up the rotational-to-linear transmissions. The cylinder and steering plants act on the *transmission plant*, which in turn outputs motion $\dot{l}_v$ in response to the *joint plant's* mediation of force f_l into f_w. In Faulring (2005) and Faulring et al. (2006a) we develop a model of the transmission plant and provide bond graphs depicting all effort and flow losses of the transmission and joint plants. The *desired cylinder speed* block computes a desired cylinder speed, ω_d, based on the desired total energy, $\mathcal{H}_d$, computed from the virtual environment. This block is described in greater detail in Section 6. The *linear-to-rotational (LTR) conversion* in Figure 16 represents Equation 6, the method by which desired joint accelerations, $\ddot{l}_d$, are turned into desired steering velocities, $\dot{\phi}_d$.

5.3. Steering

The *steering* system consists of a plant and a proportional plus integral (PI) controller with closed-loop bandwidth of 100 Hz for steering angular velocity, $\dot{\phi}$. Per Equation 6 it is necessary to control $\dot{\phi}$ to regulate joint acceleration, $\ddot{l}$. However, depending on operating conditions, if $\dot{\phi}$ is too large, the transmission may slip. Thus we require that Equation 9, $\varepsilon \mu P \geq f_w \sec(\phi)$, be satisfied. Choosing $\varepsilon < 1$ ensures that the friction force does not approach that required to cause gross slip. Next we recognize that the most significant component of f_w (see Equation 8) in our implementation is due to the joint inertia, not joint friction or operator force. Thus approximating $f_w \approx m_l \ddot{l}$ and assuming that $\dot{\omega} = 0$, combining Equations 8 and 9 along with ε yields a limit on steering velocity,

$$\dot{\phi}_{max}(\phi) = \frac{\varepsilon \mu P}{m_l R \omega \sec^3(\phi)}. \tag{10}$$

If the measured steering velocity exceeds this limit, the steering torque is pulled to zero. This has been implemented with $\varepsilon = 0.5$ and works well at preventing slip based instabilities in the transmission.

5.4. Cylinder

The *cylinder* system consists of a plant and cylinder controller containing feedback and feedforward components. The proportional plus integral (PI) feedback controller compensates for errors in cylinder velocity. The feedforward term estimates the cylinder torque required to combat friction in the device, accelerate cylinder inertia and joint masses, and

2. Depending on the steering angle of the transmission, this estimate of joint velocity has resolution ranging from far superior to approximately equivalent to the velocity signal obtained from finite differentiation of the linear potentiometer $(1 - z^{-1})/(T)l_v'$. Thus, a high-resolution joint position sensor may not be necessary for cobots to accurately determine their velocity. However, imperfections in the transmission (elastic lateral creep causing slip angles of 0.2 degrees (Faulring 2005; Faulring et al. 2006a)) cause a slight phase lag of the steering angle/cylinder speed estimate of joint velocity relative to the linear potentiometer version, but typically less than that induced by filtering the finite differentiated signal.

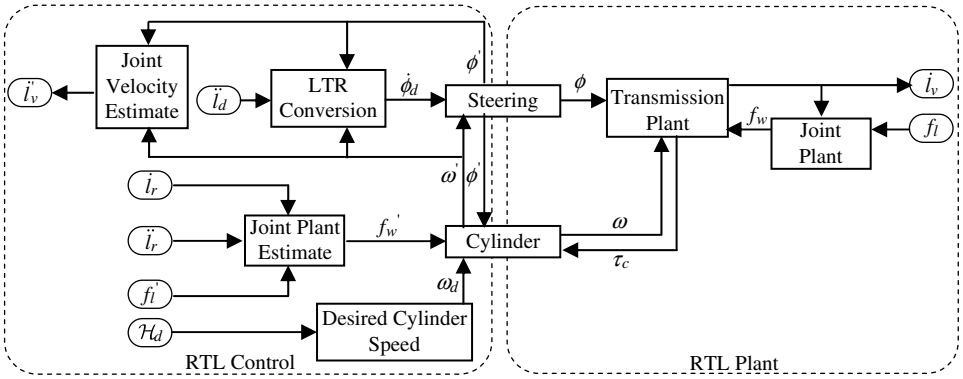

Fig. 16. The rotational-to-linear system consists of the cylinder and steering controllers and plants, the transmission and joint plants and several auxiliary control functions. Again, the $'$ notation indicates sampled (measured) signals.

oppose operator applied loads. The closed-loop system has 50 Hz bandwidth.

5.5. Control Overview With Joint-to-Task Kinematics

Finally, in Figure 17 we add in the kinematics, ϑ, such that task space accelerations of the rigid body end-effector must be mapped first to the desired joint motions. Subsequently, control is performed at a joint on joint basis.

6. Energy-tracking Controller

6.1. Motivation

The Cobotic Hand Controller utilizes the parallel architecture shown in Figure 1, which contains control redundancy. It has more actuators than task-space degrees of freedom. The speed of the power cylinder is arbitrary. This control redundancy has been addressed previously (Moore 2001; Kim 2003; Santos-Munne 1997). Here we propose a new controller that varies the power cylinder speed with respect to the total kinetic plus elastic energy of the virtual environment. We show that we are able to reduce the nominal speed of the cylinder and therefore wear of components without adversely affecting haptic display.

6.2. Total Energy Function

We cannot use Equation 6 alone to solve for steering velocities in terms of desired joint accelerations, nor can we use Equation 5 alone to solve for desired steering angles. Both represent six equations in seven unknown velocities. We solve the actuation redundancy of our six-degree-of-freedom device with seven actuators by defining an additional constraint involving cylinder surface speed. We fix cylinder surface speed,

$$R\omega = \Phi(k), \tag{11}$$

to be a function, Φ, of a ratio k. The ratio is defined as

$$k = \frac{\mathcal{H}}{R\omega}, \tag{12}$$

the ratio of the total energy of the virtual environment, $\mathcal{H}$, to cylinder surface speed, $R\omega$, and has units (kg)(m)/(s). Our total energy,

$$\mathcal{H} = \frac{1}{2}\left(\dot{q}^T M(q)\dot{q} + K(q_o - q)^T(q_o - q)\right), \tag{13}$$

is the sum of the virtual environment kinetic energy and any potential energy stored in virtual environment springs. Here $M(q)$ is the virtual environment inertia matrix and K the virtual environment stiffness matrix. Both kinetic and potential energy are considered such that the total does not change abruptly upon impacts with constraints. Energy is a particularly stable and objective metric for moving between the topology of virtual environment coordinates, q, to that of the cylinder, independent of the haptic display kinematics and configuration, x.

6.3. Desired Ratio/Cylinder Speed Trajectory

Both cylinder surface speed $R\omega$ and ratio k change with energy level $\mathcal{H}$ due to Equations 11 and 12. We visualize this via a space with abscissa k and ordinate $R\omega$ (Figures 18 and 19). Iso-contours of energy in this space are $\mathcal{H} = R\omega k$. $R\omega = \Phi(k)$ is the path we proceed along across the level curves of $\mathcal{H}$. We tend to find the best performance when the trajectory $\Phi(k)$ has the form $\Phi(k) = \sigma + (\frac{k}{\gamma})^2$, where σ is a non-zero minimum value for $R\omega$, and the quadratic term $(\frac{k}{\gamma})^2$ limits high transmission ratios and keeps the trajectory $\Phi(k)$ orthogonal to the contours of H. This avoids requiring either the cylinder or transmissions to adjust too rapidly as $\mathcal{H}$ varies. σ, the minimum value for $R\omega$, should be sufficient

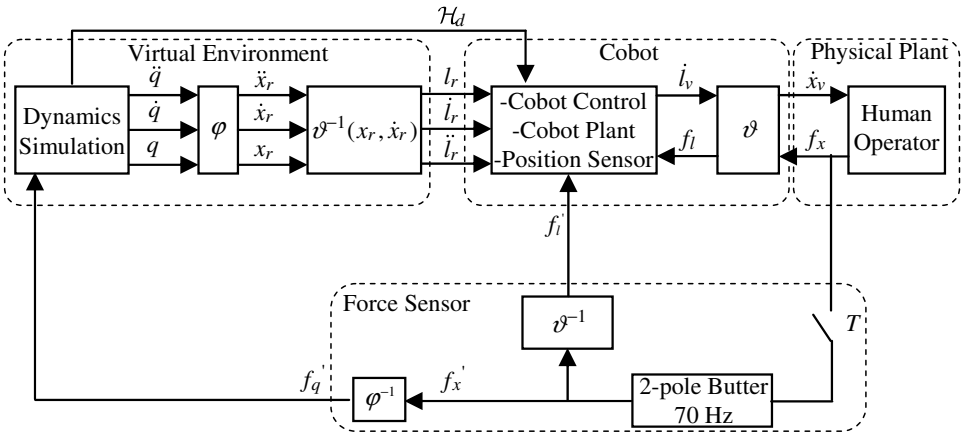

Fig. 17. The overall control diagram including kinematics. An additional set of kinematics, φ, is introduced here which transforms between coordinates in which the dynamics simulation is performed, q, and task space coordinates of the manipulandum, x. For the framework presented in Faulring (2005), ($\dim(q) \leq \dim(x)$).

to ensure that the steering actuators do not require unreasonable responses to free-motion accelerations. Thus, for a given virtual environment mass and preload force availability, we need a certain level of cylinder speed. The suggested minimum value for $R\omega$ is $\sigma = \frac{\mu P}{|M(q)|}\left(\frac{1}{f_{cyl}}\right)$ where f_{cyl} is the bandwidth of the cylinder speed controller in hertz and $M(q)$ the inertia matrix of the simulated rigid body or mechanism in the virtual environment. $|M(q)|$ for a rigid body needs to incorporate both translational mass, m_t, and rotational inertia, J_r, via a metric such as $\frac{1}{2}\left(m_t + \frac{\text{trace}(J_r)}{{r_c}^2}\right)$, where r_c is a characteristic length scale (e.g., the radius of the end-effector platform).

When we have a virtual environment model running, the vectors q, $\dot{q}$ and $\ddot{q}$ will be computed. From these vectors we can evaluate the desired $\mathcal{H}$ and $\dot{\mathcal{H}}$. Subsequently, we can solve

$$\mathcal{H} = kR\omega = k\Phi(k) \tag{14}$$

for the desired k and also the desired ω. The functions Φ may be difficult to solve for k given $\mathcal{H}$, but a simple binary search can efficiently find the solution of the monotonically increasing function we proposed for Φ. We can also differentiate Equation 14 to yield the rate of change of the total energy with respect to time,

$$\dot{\mathcal{H}} = k\frac{\partial(R\omega)}{\partial t} + R\omega\frac{\partial k}{\partial t} = k\frac{\partial\Phi(k)}{\partial k}\dot{k} + R\omega\dot{k}. \tag{15}$$

This can then be solved to yield

$$\dot{k} = \frac{\dot{\mathcal{H}}}{k\frac{\partial\Phi(k)}{\partial k} + R\omega}, \tag{16}$$

and also desired cylinder acceleration, $\dot{\omega}$.

Now we can evaluate the steering velocities by plugging Equation 12 into Equation 6 and solving for $\dot{\phi}$ in terms of k_d, $\dot{k}_d$, $\mathcal{H}_d$ and $\dot{\mathcal{H}}_d$ (note that while we dropped the subscript d in Equations 14-16, all parameters in those equations are the product of simulation and thus are desired quantities as indicated in Figures 15 and 16). In practice we drop the excitatory $\dot{\mathcal{H}}_d$ and $\dot{k}_d$ terms (they tend to make the model of the system a bit too perfect and therefore "alive"). We also neglect the use of $\dot{\omega}_d$ for the cylinder computed-torque feedforward controller, thereby providing a bit of damping. The cylinder controller does utilize ω_d for the set-point of the cylinder velocity feedback controller.

6.4. Free Motion Performance Experiment

We analyze the performance of the proposed energy-tracking cylinder speed controller during manipulation with an unimpeded mass-damper virtual environment. We manipulate a 2.0 kg mass in a 0.1 (N)/(m/s) damping environment. All three translations are allowed and rotation is disallowed. In Figure 18 we record the energy-tracking controller's performance during manipulation of this mass–damper system. The system was accelerated from a state of rest to 0.04 J, which is 0.2 m/s for a 2.0 kg mass, and then decelerated back to rest. The cylinder speed increases and subsequently decreases in surface speed, from the nominal minimum of $\sigma = 0.214$ m/s to a maximum of 0.478 m/s. Deviation between the desired and actual trajectories is due to the dynamics of the cylinder and joint motion controllers.

7. Unilateral Impact (Acceleration) Capability

We analyze the performance of the proposed energy-tracking cylinder speed controller and maximum steering velocity

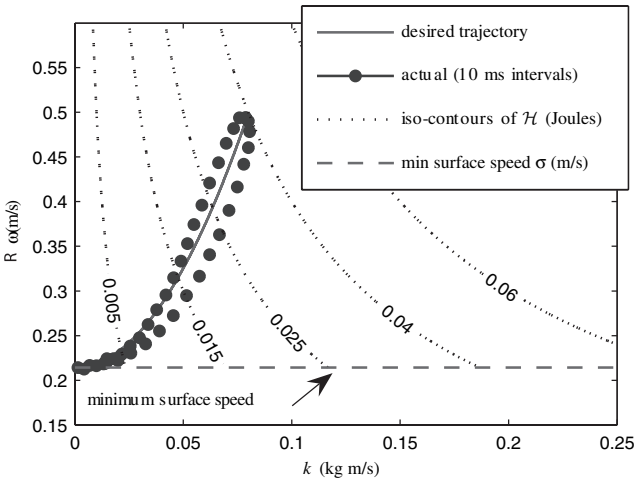

Fig. 18. Desired and actual cylinder surface speed, $R\omega$, and ratio, $k = \mathcal{H}/(R\omega)$, during interaction with a mass–damper virtual environment. Cylinder surface speed changes as a function of virtual environment energy, $\mathcal{H}$, via the desired trajectory $R\omega = \Phi(k) = 0.214 + (\frac{k}{0.15})^2$.

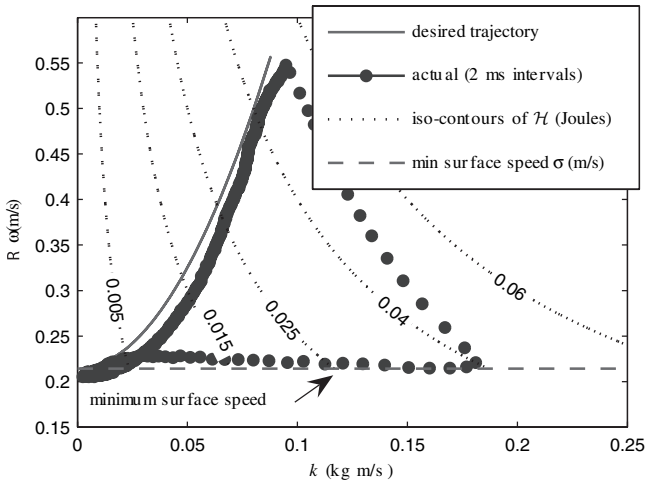

Fig. 19. Desired and actual cylinder surface speed, $R\omega$, and ratio, $k = \mathcal{H}/(R\omega)$, during a unilateral collision with a dissipative wall. Cylinder surface speed changes as a function of virtual environment energy, $\mathcal{H}$, via the desired trajectory $R\omega = \Phi(k) = 0.214 + (\frac{k}{0.15})^2$.

heuristic during manipulation in a virtual environment containing unilateral constraints. We again manipulate a 2.0 kg mass in a 0.1 (N)/(m/s) damping environment while disallowing rotations. The environment is bounded by a unilateral constraint characterized by stiffness 10,000 N/m and damping 400 (N)/(m/s). In Figures 19 and 20 we record the energy-tracking controller's performance during impact with the dissipative unilateral constraint. The desired trajectory in Figure 19 is followed relatively well until the constraint is encountered. When the constraint is encountered, the cylinder is able to reduce speed much quicker than the joints are able to reduce their energy (compare the delays in subplots A and B of Figure 20). The actual trajectory in Figures 19 and 20, based on measured joint velocities and positions, stays at a much higher energy level than the near-zero energy level requested after simulation of a dissipative impact. The actual and desired cylinder speeds have returned to σ, but the actual energy level, H, has not returned to zero as the joints are still moving. Even as the wheels steer to stop the joints, creep and slip occur since the wheels incur heavy loads decelerating the joint masses and resisting the operator applied forces. The result is performance that does not coincide with the 40 Hz motion control bandwidth of the joints.

This apparent lack of performance is analyzed in Figure 21 where the deviation between desired and actual end-effector position during the unilateral impact of Figures 19 and 20 is shown. Note that the desired trajectory penetrates the wall only about 1.0 mm while the actual penetration is 3–4 mm (Figure 21). The walls are initially soft (the 3–4 mm pene-

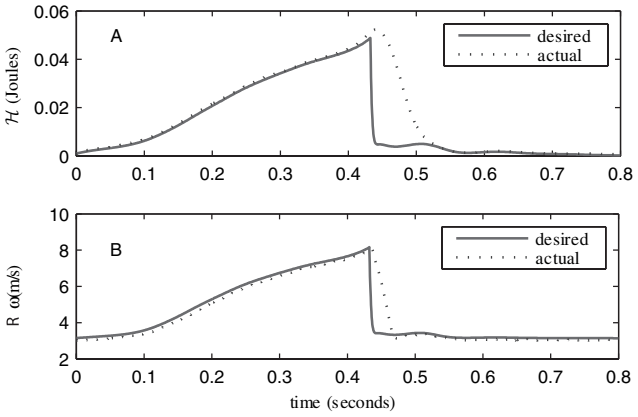

Fig. 20. A. Desired and actual (measured) total energy of virtual environment during a unilateral collision with a dissipative wall. The desired total energy is computed from the desired inertia, positions and velocities. The actual total energy is computed from the desired inertia but the actual (measured) positions and velocities. B. Desired and actual cylinder surface speed. The controller succeeds in achieving high cylinder speeds at times of impact with unilateral constraints when small steering angles are needed to sustain the forces required for high joint accelerations. The high cylinder speed and resulting small steering angles reduce the lateral loads on the wheel, decreasing the probability of slip.

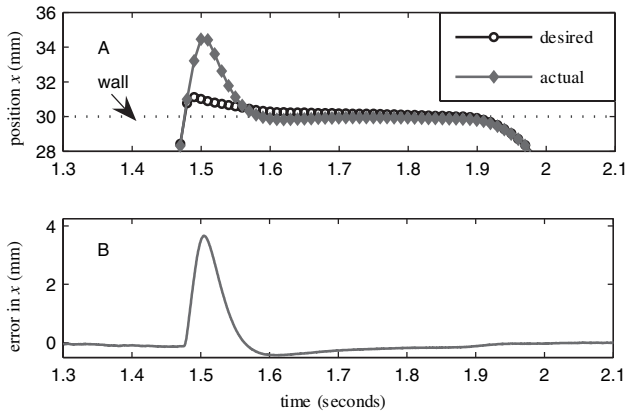

Fig. 21. On the left is fixed cylinder speed and on the right is the variable cylinder speed algorithm. The user is moving a ball between walls located at ±30 mm.

tration rather than the desired 1 mm penetration) but harden quickly as the user is pushed back to the wall, even when applying a significant load. The resulting haptic perception is of a soft wall (1 to 3 kN/m) that hardens quickly after impact (i.e., faithfully reproducing the requested 10,000 N/m at times of low acceleration). This contrasts with impedance displays that can use impulses to create the perception of a hard initial contact, and are then unable to sustain high forces (Salcudean and Vlaar 1997). This particular simulation and set of initial conditions demands about 34 m/s^2 acceleration while only a 7.4 m/s^2 acceleration is delivered by the cobot. Since the cobot is capable of approximately 30 m/s^2 provided the wheels are at $\phi = 0$ (and allowed 15 m/s^2 for $\varepsilon = 0.5$ in the linear slip prevention heuristic of Equation 10), there is some margin for controller development. We would like to increase the gains in order to be able to achieve the maximum allowed acceleration of 15 m/s^2, however this leads to excitation of structural dynamics and to wheel slip. Nevertheless, achieving 7.4 m/s^2 out of a limit of 15 m/s^2, is perhaps the best that can be expected given the numerous controllers and plants involved. While the 95%rise-time of 0.1 seconds may seem slow for a system with 40 Hz capability, the maximum steering velocity heuristic and creep/slip in the transmissions limit the acceleration for this abrupt step input (which nominally asks for discontinuous acceleration).

The fact that the finite preload, and therefore finite acceleration capacity limits the unilateral contact performance can perhaps be addressed via an event-based solution (Kuchenbecker et al. 2005). Impulsive solutions like those suggested by Salcudean and Vlaar (1997) and Mirtich and Canny 1995) cannot be used for this system, since we can only achieve a limited acceleration and applying an impulse to the cylinder or steering motors results in slip. This slip limits the achievable accelerations of the Cobotic Hand Controller by causing a positive feedback loop. As slip occurs, more steering is requested which only compounds the issue. Event-based feedforward routines might do well, ignoring both the resonance of structural dynamics and the nonlinear disaster of creep/slip of the rolling wheel, by simply playing back a steering trajectory independent of joint motion control.

8. Z-width Exploration

8.1. Methods

We establish the range of virtual admittances or impedances that the cobot can stably render, the Z-width (dynamic range) of Colgate and Brown (1994) and Brown and Colgate (1998), as a function of the mechanical impedance the end-effector contacts. Figure 22 depicts the method by which the data is obtained for this experiment. The virtual environment of the system consists of a virtual spring, $k_{virtual}$, a virtual damper, $b_{virtual}$, and a virtual mass, $m_{virtual}$. If the actual cobot and virtual systems move to locations, $x_{physical}$, and $y_{virtual}$, the real spring, $k_{physical}$, generates a load, f_{sensor}, at the load cell. Similar testing protocols have been implemented by others for determining the stable impedance range of a haptic display (Colgate 1988; Ellis et al. 1996; Eppinger 1988; Moreyra and Hannaford 1998). The simulation is oriented along the axis of the cylinder, rendering the motion of all six joints identical. The experiment was performed with the nominal cylinder speed set at 5.0 rad/s, and with the maximum steering velocity heuristic actively limiting steering torque if $\dot{\phi}_{max}$ was to be exceeded. The test protocol required the end-effector to be brought into contact with the real spring by moving along the axis of the cylinder at 5 cm/s until a 5 N load was detected. The zero point of the virtual spring is set at this location. After a 0.25 s delay, the virtual environment simulation was started and a stability metric applied.

We tested four different virtual masses over a range of virtual damping and virtual stiffness. In addition, the whole experiment was performed with three different physical springs, $k_{physical}$. The first spring was a 1000 N/m die spring, approximately 30 cm long and 3.5 cm in diameter, which was slid onto a cylinder for support as it lay horizontally. The second spring was a 3000 N/m die spring, also 30 cm long and 3.5 cm in diameter, and again slid onto a cylinder for support as it lay horizontally. The third was a 6000 N/m piece of 12 mm thick, 40 durometer polyurethane. The stability metric and exploration algorithm are explained in greater detail in Faulring (2005).

8.1. Results

In Figure 23 we plot the results of the Z-width exploration tests for the three physical springs examined. Depending on the impedance that the Cobotic Hand Controller is interacting

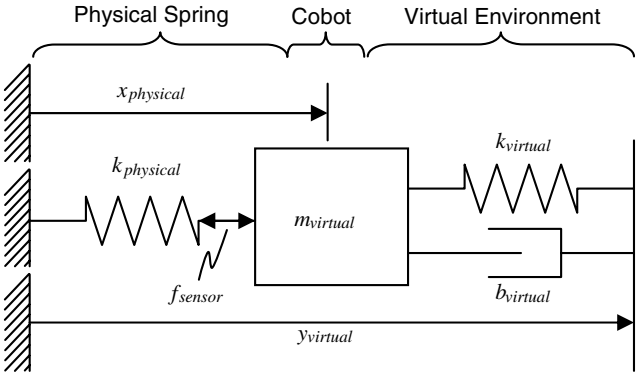

Fig. 22. Schematic of admittance display system. The virtual environment gives the desired impedance, or interaction behavior of the cobot with the physical environment.

with, the stable virtual impedances it can render are characterized by a top stable natural frequency between 15 and 40 Hz (if we form a second- order system from $m_{virtual}$, $k_{virtual}$ and $b_{virtual}$). The minimum useful impedance is around 2 kg with zero damping, although a "careful" user is capable of manipulating a 0.1 kg mass with zero damping. The 2 kg mass need not have any weight (zero virtual gravity), so the operator feels only the inertial forces which are small for low accelerations. The dynamic range of the Cobotic Hand Controller is large for a haptic display. Virtual stiffness values as high as 100 kN/m were stably rendered, and while at zero stiffness the simulation is stable with near zero damping.[3]

Regardless of the impedance, $k_{physical}$, that the end-effector contacted, increasing the mass, $m_{virtual}$, always led to higher stable stiffness, $k_{virtual}$, and to a larger range of stable values for damping, $b_{virtual}$. Increasing the impedance, $k_{physical}$, from a 1000 N/m to a 3000 N/m die spring led to a reduced stiffness that could be stably rendered. However, with the additional damping of the polyurethane, the 6000 N/m 40 durometer pad was as stable as the 1000 N/m die spring, even in the absence of virtual damping. An exception was the 0.158 kg virtual mass, which had no stable values for the polyurethane pad. For a small virtual mass, the resulting high accelerations caused torque saturation of the steering control which led to instability. The high desired joint accelerations that result from using a small mass also led to slip-based instabilities that escaped the steering velocity heuristic.

The stable impedance range of the Cobotic Hand Controller is limited by steering dynamics and transmission creep/slip. Steering dynamics produce a phase lag relative to the virtual environment that tends to help filter out high frequency content from transmitting from the virtual environment to the proximal and distal links. However, creep, and, in the worst case, slip, occurs in the transmission when it attempts to accelerate/decelerate the inertia of a link. This slip causes a deviation between the reference and virtual positions, and large feedback errors are generated that require even larger steering velocities. In addition, the high frequency content of a slip occurrence will excite the structural resonances of the proximal and distal links. We believe that slip is the mechanism that ultimately limits the range of impedances that can be stably rendered.

3. If the structural stiffness of the Merlet platform is taken into account, these 100 kN/m software levels may in actuality only be 20 kN/m, depending on configuration.

9. Conclusions

We have designed and built an active six-degree-of-freedom cobotic haptic display with force transmission capabilities exceeding 50 N, structural stiffness ranging from 20–400 kN/m, a motion control bandwidth of 40 Hz, and near zero power requirements for sustaining high output loads. Based on our experience with haptic interface devices, the dynamic range of this display is quite broad. Although the Cobotic Hand Controller is controlled as an admittance device, allowing motions based on the applied force, the cobot does not suffer from the high inertia, friction and backlash that normally exist in a highly geared admittance device. The crisp distinction between free and forbidden directions of motion is striking. This performance arises not from elaborate control algorithms, but from the inherent physical characteristics of the device due to the utilization of non-holonomic rolling constraints. In order to render constraints on motion, the device controls the steering motion of transmissions rather than attempting to match an actuator torque to an operator applied effort. The result is a highly power efficient display that requires only a few watts of electrical power even while imparting high stiffness values and forces to the user. A key design choice, which enabled the display of high stiffness values and crisp constraints, was the use of steel-on-steel precision-ground bearing quality components in dry-friction rolling contact. This choice yielded transmissions with high bandwidth, near-zero rolling friction, zero backlash and near-zero compliance.

We have introduced many innovations to cobot control in our design of a control architecture for the Cobotic Hand Controller. We designed an admittance architecture for cobots based on commanding acceleration rather than curvature. We developed a novel energy-tracking cylinder speed controller that reduces wear and vibration without degrading haptic performance. We designed a maximum steering velocity heuristic to prevent transmission slip that leads to instability. We then presented results of stable dynamic range exploration with the Cobotic Hand Controller. Future cobot control improvements should strive to maximize the range of impedance by fully utilizing acceleration capability, particularly during unilateral impacts. As mentioned in Section 7, it may be useful to pursue an event-based solution to unilateral impacts by simply

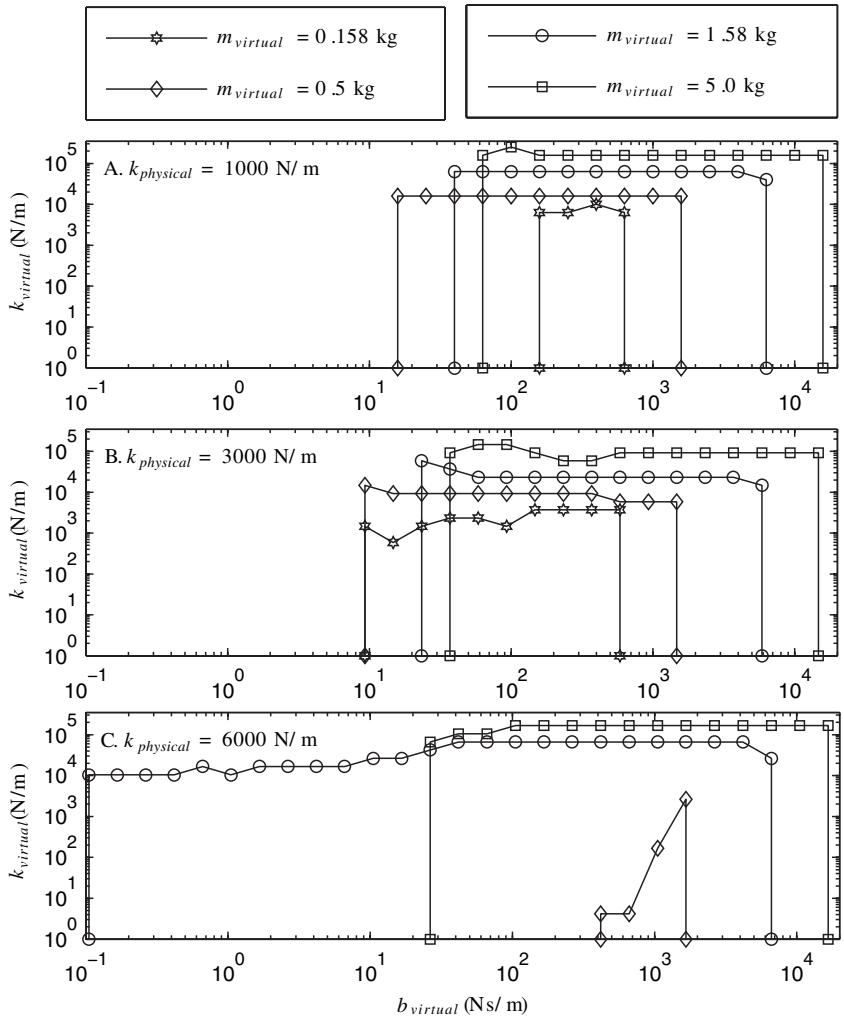

Fig. 23. Stability regime in the virtual stiffness and virtual damping plane for various virtual inertias. A. Physical impedance $k_{physical}$ = 1000 N/m die spring. B. Physical impedance $k_{physical}$ = 3000 N/m die spring. C. Physical impedance $k_{physical}$ = 6000 N/m 40 durometer polyurethane pad. There were no stable points for $m_{virtual}$ = 0.158 kg with the polyurethane.

playing back a steering trajectory independent of joint motion control.

We envision parallel cobots as an enabling technology for haptics and prosthetics that will allow for increases in the dynamic range of these devices while simultaneously permitting reductions in actuator size and power requirements. Use of a CVT eliminates the need to make compromises on output flow and effort, which are inherent to choosing a fixed transmission ratio. The result is mechanisms with enhanced dynamic range that extends continuously from a completely clutched state to a highly backdrivable state.

Many pictures and videos of the Cobotic Hand Controller and its rendering of virtual environments are available at the Laboratory for Intelligent Mechanical Systems Web site at http://lims.mech.northwestern.edu/projects/handcontroller/.

Acknowledgment

The authors would like to thank Young Park, Tom Ewing and Hyosig Kang for their contributions to this research. This work was supported by the DOE grant number DE-FG07-01ER63288.

References

Abbott, J.,Hager, G., and Okamura, A. 2003. Steady-hand teleoperation with virtual fixtures. *12th IEEE International Workshop on Robot and Human Interactive Communication*, pp. 145–151.

R. Adams, M. Moreyra, and B. Hannaford. Excalibur, a three-axis force display. *ASME Winter Annual Meeting Haptics Symposium*, Nashville, TN, 1999, pp. 465–474.

Adelstein, B. and Rosen, M. 1992. Design and implementation of a force reflecting manipulandum for manual control research. *Advances in Robotics, ASME DSC* 42:1–12.

Arai, H. 1996. Controllability of a 3-DOF manipulator with a passive joint under a nonholonomic constraint. *IEEE International Conference on Robotics and Automation*, Minneapolis, MN, pp. 3707–3713.

Argonne National Laboratory. 1998. Dual arm work platform teleoperated robotics system. Department of Energy, Technical Report DOE/EM-0389.

Brown, J. and Colgate, J. 1997. Passive implementation of multibody simulations for haptic display. *ASME IMECE DSC* 61:85–92.

Brown, J. and Colgate, J. 1998. Minimum mass for haptic display simulations. *ASME IMECE DSC*, pp. 249–256.

Carignan, C. and Cleary, K. 2000. Closed-loop force control for haptic simulation of virtual environments. *Haptics-e*, 1(2):1–14.

Chuckpaiwong, I. 2001. Reflexive collision avoidance for a novel parallel manipulator. Masters Thesis, Case Western Reserve University.

Colgate, J. 1988. The control of dynamically interacting systems. PhD Dissertation, Massachusetts Institute of Technology.

Colgate, J. and Brown, J. 1994. Factors affecting the Z-width of a haptic display. *IEEE International Conference on Robotics and Automation*, San Diego, CA, pp. 3205–3210.

Colgate, J. and Peshkin, M. 1999a. US Patent No. 5923139: Passive robotic constraint devices using nonholonomic transmission elements. Patent.

Colgate, J. and Peshkin, M. September 1999b. US Patent No. 5952796: Cobots. Patent.

Ellis, R., Ismaeil, O., and Lipsett, M. 1996. Design and evaluation of a high-performance haptic interface. *Robotica* 14(3):321–327.

Emrich, R. and Hodgson, A. 2000. A translational-to-rotational continuously variable transmission element for a parallel cobot. *ASME IMECE DSC*, 69:1285–1292.

Eppinger, S. 1988. Modelling robot dynamic performance for endpoint force control. PhD Dissertation, Massachusetts Institute of Technology,

Faulring, E. 2005. The cobotic hand controller: Design, control and analysis of a novel haptic display. PhD Dissertation, Northwestern University.

Faulring, E., Colgate, J., and Peshkin, M. 2004. A high performance 6-DOF haptic cobot. *IEEE International Conference on Robotics and Automation*, New Orleans, LA, pp. 1980–1985.

Faulring, E., Colgate, J., and Peshkin, M. 2006a. Power efficiency of the rotational-to-linear infinitely variable cobotic transmission. Accepted by *ASME Journal of Mechanical Design*.

Faulring, E., Lynch, K., Colgate, J., and Peshkin, M. 2005. Haptic interaction with constrained dynamic systems. *IEEE International Conference on Robotics and Automation*, Barcelona, Spain.

Faulring, E., Lynch, K., Colgate, J., and Peshkin, M. 2006b. Haptic display of constrained dynamic systems via admittance displays. Accepted by *IEEE Transactions on Robotics*.

Force Dimension. Delta Haptic Device,February 2004, http://www.forcedimension.com/fd/avs/home/products/6-dof_delta/.

Gillespie, R., Colgate, J., and Peshkin, M. 2001. A general framework for cobot control. *IEEE Transactions on Robotics and Automation* 17(4):391–401.

Grace, K. 1995. Kinematic design of an ophthalmic surgery robot and feature extracting bilateral manipulation. PhD Dissertation, Northwestern University.

Hannaford, B. 1989. A design framework for teleoperators with kinesthetic feedback. *IEEE Transactions on Robotics and Automation* 5(4):426–434.

Hayward, V. and Astley, O. 1996. Performance measures for haptic interfaces. *Robotics Research: The 7th International Symposium*, pp. 195–207.

Joly, L. and Andriot, C. 1995. Imposing motion constraints to a force reflecting telerobot through real-time simulation of a virtual mechanism. *IEEE International Conference on Robotics and Automation*, pp. 357–362.

Kim, S. 2003. Control of the powered arm cobot and analysis of the rotational CVT. PhD Dissertation, Northwestern University.

Kim, K., Chung, W., and Youm, Y. 2003. Design and analysis of a new 7-DOF parallel type haptic device: PATHOS-II. *IEEE/RSJ International Conference on Intelligent Robots and Systems*, Las Vegas, NV.

Kuchenbecker, K., Fiene, J., and Niemeyer, G. 2005. Event-based haptics and acceleration matching: Portraying and assessing the realism of contact. *First Joint Eurohaptics Conference and Symposium on Haptic Interfaces for Virtual Environment and Teleoperator Systems*, Pisa, Italy.

Lee, C., Lawrence, D., and Pao, L. 2000. A high-bandwidth force-controlled haptic interface. *Symposium on Haptic Interfaces for Teleoperation and Virtual Reality, ASME IMECE*.

Massie, T. and Salisbury, J. 1994. The PHANTOM haptic interface: A device for probing virtual objects. *ASME Winter Annual Meeting, Symposium on Haptic Interfaces for Virtual Environment and Teleoperator Systems*, Vol. DSC 55,

Chicago, IL, pp. 295–302.

Merlet, J. 1991. U.S. Patent No. 5053687: Articulated device for use in particular in robotics.

Merlet, J. 1992. Direct kinematics and assembly modes of parallel manipulators. *International Journal of Robotics Research* 11(2):150–162.

Millman, P. and Colgate, J. 1991. Design of a four degree-of-freedom force reflecting manipulandum with a specified force-torque workspace. *IEEE International Conference on Robotics and Automation*, Sacramento, CA, pp. 1488–1493.

Mirtich, B. and Canny, J. 1995. Impulse-based simulation of rigid bodies. *Symposium on Interactive 3D Graphics*, pp. 181–188.

Moore, C. 2001. Design, construction, and control of a 3-revolute arm cobot. PhD Dissertation, Northwestern University.

Moore, C., Peshkin, M., and Colgate, J. 2003. Cobot implementation of virtual paths and 3D virtual surfaces. *IEEE Transactions on Robotics and Automation* 19(2):347–351.

Moreyra, M. and Hannaford, B. 1998. A practical measure of dynamic response of haptic devices. *International Conference on Robotics and Automation*, Leuven, Belgium, pp. 369–374.

Morris, D. 2001. Experiments in mechanical assembly using a novel parallel manipulator. Masters Thesis, Case Western Reserve University.

Noakes, M., Love, L., and Lloyd, P. 2002. Telerobotic planning and control for DOE D&D operations. *IEEE International Conference on Robotics and Automation*, Washington DC, pp. 3485–3492.

Peshkin, M., Colgate, J., Wannasuphoprasit, W., Moore, C., Gillespie, R., and Akella, P. 2001. Cobot architecture. *IEEE Transactions on Robotics and Automation* 17(4):377–390.

Quanser. 3 DOF Planar Pantograph. August 2005, http://www.quanser.com/english/html/products/.

Rosenberg, L. 1994. Virtual fixtures: Perceptual overlays enhance operator performance in telepresence tasks. PhD Dissertation, Stanford University.

Salcudean, S. and Vlaar, T. 1997. On the emulation of stiff walls and static friction with a magnetically levitated input-output device. *ASME Journal of Dynamics, Measurement and Control* 119:127–132.

Salisbury, K., Eberman, B., Levin, M. and Townsend, W. 1990. The design and control of an experimental whole-arm manipulator. *The Fifth International Symposium on Robotics Research*, pp. 233–241.

Santos-Munné, J. 1997. Extreme joystick: A cobot with stored energy. PhD Proposal, Mechanical Engineering Department, Northwestern University.

Sensable Technologies. PHANTOM Devices. March 2006, http://www.sensable.com/products/phantom_ghost/phantom.asp.

Sheridan, T. 1992. *Telerobotics, Automation, and Human Supervisory Control*. MIT Press, Cambridge, MA.

Tan, H., Eberman, B., Srinivasan, M., and Cheng, B. 1994. Human factors for the design of force-reflecting haptic interfaces. *ASME DSC* 55(1):353–359.

Van der Linde, R., Lammertse, P., Frederiksen, E., and Ruiter, B. 2002. The HapticMaster, a new high-performance haptic interface. *EuroHaptics*, Edinburgh, UK.

Wang, Y. 1999. Workspace analysis of a novel closed-chain manipulator. Masters Thesis, Case Western Reserve University.

Wannasuphoprasit, W., Gillespie, R., Colgate, J., and Peshkin, M. 1997. Cobot control. *International Conference on Robotics and Automation*, Albuquerque, NM, pp. 3571–3576.

Yoshikawa, T. 2000. Force control of robot manipulators. *IEEE International Conference on Robotics and Automation*, San Francisco, CA, pp. 220–226.